

Comparative Study of the Performance Improvement of an Axial Compressor with a Micro-Vortex Generator and a Suction Slot

S. Ma¹, X. L. Sun^{†2}, W. Cheng² and W. L. Chu³

¹ College of Flight Technology, Civil Aviation Flight University of China, Guanghan, Nanchang Road, 618307, China

² College of Aeronautical Engineering, Civil Aviation Flight University of China, Guanghan, Nanchang Road, 618307, China

³ School of Power and Energy, Northwestern Polytechnical University, Xi'an, Youyi West Road, 710129, China

†Corresponding Author Email: cafuc_sxl@163.com

(Received November 08, 2022; accepted February 1, 2023)

ABSTRACT

Flow control methods have been gradually applied to improve the flow field characteristics of axial compressors. However, most of the current research is focused on the cascade, and few studies have taken a compressor as the research object. Therefore, a 3.5-stage transonic axial compressor is adopted to explore the characteristics of different flow control schemes. The effects of the micro-vortex generator (MVG), segmented boundary layer suction (BLS), and combined technology (COM) on the MVG and BLS are compared by the numerical simulation method. The research results are summarized as follows. The excessive accumulated low-energy fluid in the blade passage induces the occurrence of a corner stall in the last stage stator of an axial compressor. At this time, the compressor can still work, but the performance has accelerated deterioration. The flow characteristics are effectively improved when the MVG is introduced, the stall margin improvement ΔSM and the peak efficiency improvement $\Delta \eta_e$ of the last stage are 2.1% and 1.02%, respectively. Moreover, the BLS shows advantages in removing the three-dimensional reverse flow and decreasing the total pressure loss compared with the MVG, the ΔSM of the last stage is 2.69%, and the $\Delta \eta_e$ is 1.83%. When the combined technology is applied, it shows a significant advantage in delaying the occurrence of a corner stall, and the stall margin of the last stage is improved by 2.71%. Based on a quantitative analysis method using loss sources, the three flow control schemes show significant advantages in reducing the secondary flow loss sources and the wake loss sources. Above all, the BLS shows significant advantages in reducing the total pressure loss, and the COM shows an advantage in expanding the stable operating range. The research results will provide a reference for studies of flow control methods related to reducing flow losses and widening stability margins.

Keywords: Corner separation; Stable operating range; Combined flow control technology; Segmented suction slot; Micro-vortex generator.

NOMENCLATURE

MVG	Micro-Vortex Generator	δ	boundary layer thickness
BLS	Segmented Boundary Layer suction	h_T	height of the MVG
COM	combined technology between MVG and BLS	l_{VG}	chord length of the MVG
LE	Leading Edge	d_{VG}	blade space of the MVG
TE	Trailing Edge	θ_{VG}	blade profile angle of the MVG
h_{R3}	height of the rotor blade	β_{VG}	stagger angle of the MVG
h_{S3}	height of the stator blade	Z_{BLS}	installation position of the suction slot
C_{R3}	chord length of the rotor blade	$\Delta \eta_e$	peak efficiency improvement
C_{S3}	chord length of the stator blade	$\Delta \eta_{e13suc}$	peak efficiency improvement considering the suction flow
P_{R3}	pitch of the rotor blade	$(\eta_e)_{BS}$	peak efficiency of the baseline
P_{S3}	pitch of the stator blade	$(\eta_e)_{IM}$	peak efficiency of the optimized compressor
AR	aspect ratio		

C	chord length	BS	baseline
π	total pressure ratio	IM	optimized compressor
π_s	pressure ratio at the near-stall condition	S	near-stall condition
π_0	pressure ratio at the designed operating point	w_{LE}	relative velocity of Stator3's LE
π_{suc}	total pressure ratio at the plenum exit to RS ₃	w_{TE}	relative velocity of Stator3's TE
P	static pressure	Δw_u	swirl velocity of stator3
P_t	total pressure	τ	solidity of stator3 at root
$P_{t_{suc}}$	total pressure of the plenum exit	ρ_{in}	average density of inlet section
η	isentropic efficiency	v_m	velocity component of airflow in the main flow direction
η_{13suc}	isentropic efficiency considering the suction flow	$v_{in,C}$	average chordwise speed of inlet section
k	specific heat ratio	γ_{Pro}	profile loss source
T	total temperature	γ_{Sec}	secondary flow loss source
T_{suc}	total temperature of the plenum exit	γ_{Wake}	wake loss source
\dot{m}	mass flow rate	γ_{Corn_Hub}	corner loss source near the hub
\dot{m}_s	mass flow rate at the near-stall condition	γ_{Corn_Shr}	corner loss source near the shroud
\dot{m}_0	mass flow rate at the designed operating point	γ_{Wall_Hub}	end wall loss source near the hub
\dot{m}_{suc}	mass flow rate at the plenum exit	γ_{Wall_Shr}	end wall loss source near the shroud
ζ	total pressure loss coefficient	Φ	dissipation function
V_m	mainstream velocity	μ_{eff}	effective viscosity coefficient
SM	surge margin	μ	laminar viscosity coefficient
ΔSM	stall margin improvement	μ_t	turbulent viscosity coefficient
		γ_{source}	loss source in a designated range
		$source$	loss source
		$region$	designated flow field

1. INTRODUCTION

The internal flows of a high-load axial compressor present a complex flow patterns and the interaction among the various three-dimensional flow structures ultimately affects the compressor performance. In particular, the flow fields are most complex near the end wall. These complex flows are the main reasons for a compressor to enter an unsteady flow condition, which leads to the occurrence of a stall. In recent years, scholars have carried out a large quantity of research studies to reduce the flow loss and enhance the stable operating range of compressors. These research approaches include optimization design (Smith 2002), blade/end wall structure optimization (Jonas *et al.* 2018; Stürzebecher *et al.* 2018; Vanti *et al.* 2018.), and flow control methods (Alexander *et al.* 2011; Meng *et al.* 2018; Saito *et al.* 2018). These methods effectively improve compressor performances.

However, the self-weight of a compressor is usually increased by these methods, but these methods are widely used because of their advantages such as simple design processes and easy implementation. Flow control methods mainly includes two categories (Saito *et al.* 2018). One type of method requires the introduction of external airflow to do word, and these methods are called active flow control methods. The other type of method can change the flow state of airflow by changing the structure of the blade passage, and these methods are called passive flow control methods. This method does not require the consumption of external energy, so it shows strong feasibility.

In axial compressors, a vortex generator (VG) has been widely used. It is a type of passive flow control technology, and the working process is as follows. When the air flows through a vortex generator with an installation angle, high speed induced vortices

(IV) are formed at the tip of the vortex generator. When the IV moves backward, the momentum exchange occurs in the range between the low velocity airflow and the main stream. The injection of high energy increases the energy of the boundary layer, and controls the flow separation.

Hergt *et al.* (2008) took a cascade as the experimental research object. A scheme was proposed to control the corner separation by using a vane-type vortex generator, and the relationship between the dimension of the vortex generator and the boundary layer was discussed. The results showed that if the vortex generator can show significant advantage, the height is needs to be lower than the thickness of incoming boundary layer, and the 0.25 times boundary layer thickness is the best. In 2014, Diao *et al.* (2014) took a cascade as the research object by numerical simulation. The study showed that when the VG's height was 0.3 times the thickness of incoming boundary layer, the total pressure loss is significantly decreased. Generally, when the height of a VG is 0.1–0.5 times incoming boundary layer thickness, it can be called a micro vortex generator (MVG) (Dawen *et al.* 2014). Many studies have shown that the an MVG can continuously provide sufficient momentum conversion and effectively control the flow separation and reduce the flow resistance (Lin 2002, Lin *et al.* 1991).

However, many studies have adopted the boundary layer suction (BLS) on the blade suction side to repress the corner separation in the axial compressor, such as full-span suction slot researched by Godard *et al.* (2012), as well as the segmented suction slot researched by Ding *et al.* (2017) and the suction hole (Ding *et al.* 2013). Ding Jun proposed that the full-span suction slot showed excellent capability in reducing the low speed airflow near the mid-span (Ding *et al.* 2017). However, most of the studies have only focused on analyzing the influence of the

position, shape and suction capacity of suction slot on the compressor characteristic. Few scholars have paid attention to the influences of suction slot on the compressor performance at low flow rate/large incidence conditions, especially the ability to improve the stall margin.

Therefore, to discuss the influence of different flow control methods on the internal flow of compressor and the improvement of stall margin, this work analyzes the ability of MVG to control the corner separation and takes into account the characteristics of suction slot affecting the airflow. Additionally, the impact of the combination scheme composed by the MVG and BLS on the performance of the axial compressor is studied further.

This research is mainly based on the structural characteristics and formation mechanism of a corner stall. The main research objectives are listed as follows:

1. We reveal the influence of a corner stall in the last stage stator on the performance of a transonic axial compressor.
2. We explore the ability of different flow control schemes to suppress the corner separation in the last stage stator.
3. We discuss the advantages of different flow control methods using a quantitative analysis method.

2. THE RESEARCH OBJECT

In an axial compressor, more low-energy fluid can easily accumulate on the region near the end wall of the last stage, resulting in the blockage of the blade passage (Taylor and Miller 2015). To analyze the influences of flow control methods on a compressor, the research object is a 3.5-stage transonic axial compressor. More flow blockage in the compressor can be found in the corner region of the last stage stator. Therefore, the flow fields of the last stage stator (Stator 3) improved by different flow control methods are adopted to research the performance changes of the last stage.

Although the performances of the last stage stator are the main research object in this study, in order to obtain the real flow characteristics and development process of the corner separation, all of the cases are simulated using the computational domain of the integral compressor (3.5-stage).

A total pressure is set at the inlet, given as 101325 Pa, and the total temperature is 282K. The outlet boundary is a static pressure that changes the flow rate of the blade passage by the adjustable static pressure. The calculation domain is a single passage, and the circumferential boundary of the passage is set as rotational periodicity. The surfaces of the blade, hub, and casing are set as no-slip walls.

Figure 1 is a diagram of the third stage of the compressor, and the key geometric parameters are displayed. The heights of the rotor blade and stator blade are represented by h_{R3} and h_{S3} , respectively, and the data are adopted from the LE (leading edge)

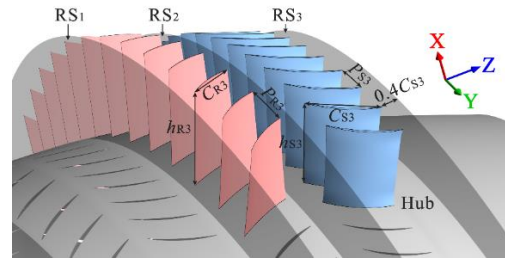


Fig. 1. The 3D schematic diagram of the last stage in the compressor.

Table 1 Geometric parameters of rotor and stator in the third stage.

Parameters	Rotor 3	Stator 3
Aspect ratio, AR	1.2	1.2
Solidity of blade root	1.46	1.63
Chord length, C /(mm)	60.1	52.2

of the blades. The chord lengths of the rotor and stator are C_{R3} and C_{S3} , and the pitches are P_{R3} and P_{S3} , respectively. RS_1 and RS_2 are the locations of the rotor-stator interface. RS_3 is a data extraction plane for compressor performance analysis, and it is on the downstream of the TE (trailing edge) of the third stage stator blade with 0.4 times the chord length of C_{S3} . At the maximum efficiency point of the third stage, the average inlet (RS_1) Mach number is about 0.78. The circumferentially-averaged outlet (RS_3) flow angle is approximately -0.072° . This means that the airflow flows out along the chordal direction. To ensure the full development of the airflow in the outlet passage, the axial length of the outlet passage is three times the length of C_{S3} . The key geometric parameters of the third-stage rotor and stator are given in Table 1.

3. NUMERICAL METHODS

The 3.5-stage axial compressor has no experimental data used to verify the reliability of numerical calculation. Thus, the task of this section is to verify the numerical methods of NASA stage 35 with open experimental data and apply the verified grid topology, grid number, turbulence model, boundary conditions, and other parameters to ensure the accuracy of the numerical calculation for the 3.5-stage axial compressor.

As shown in Fig. 2, the calculation domain of the NASA stage 35 model used for numerical verification is a single passage. The design rotation speed is 17188 RPM, and the design flow rate is 20.188 kg/s (full passages). The design total pressure ratio is 1.82. The design isentropic efficiency is 0.828. The number of rotor blades is 36, the aspect ratio is 1.19. The tip clearance of the rotor is 0.86% of the chord length. The number of stator blades is 46, the aspect ratio is 1.26, and the length of the outlet blade passage is twice of the axial chord length of the stator.

The experimental measurement of the NASA stage 35 model was carried out by Reid and Moore (1978), but only a slight amount of performance data could

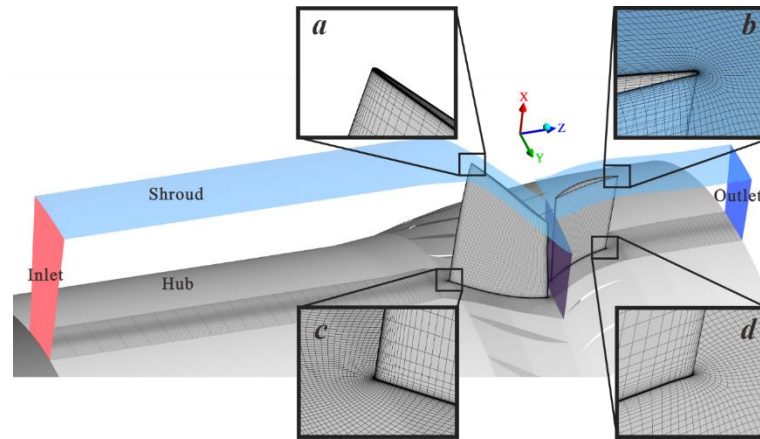


Fig. 2. Boundary conditions and grid of NASA stage 35 with a single-passage computing domain.

be found in the report. Most scholars have completed some meaningful research based on these data (Chima 2009; Yue and Wang 2018), which is enough to show that the experimental data in Fig. 4 and Fig. 5 are sufficient to verify the numerical simulation method.

In this research, the numerical simulations are conducted by the commercial solver ANSYS CFX, and the meshes are generated by AutoGrid5 and IGG. In view of the advantages of the turbulence model Shear Stress Transport (SST) in the turbomachinery simulation (Ma *et al.* 2019a, Dejour and Vo 2015, Sun *et al.* 2021a), the SST is used for the grid independence verification of NASA stage 35, and the advection scheme and turbulence model are set to a high-resolution scheme. In Fig. 2, the details of the grid topology are shown in the partially enlarged views. The blade is surrounded by O-type grid topology, and the rotor tip clearance is filled with a butterfly grid. The height of the first layer grid near the wall needs to be set to 1×10^{-6} m to guarantee the near wall $y^+ < 1$.

The boundary conditions are given in Fig. 2. The inlet boundary condition is a pressure inlet. The total pressure is 101325 Pa. The total temperature is 288.15 K. The outlet boundary condition is a static pressure outlet, and the flow rate of the compressor is controlled by the adjustable exit static pressure. The blade, hub, and casing are set to no-slip wall conditions. To save computational costs and confirm the reliability of the numerical results, it is necessary to verify the independence of the grid number. The extraction position of the numerical calculation parameters is consistent with the experiment. The three measurement positions are shown in Fig. 3. These measurement positions are position 1 upstream of the rotor blade, position 2 at the rotor-stator interface, and position 3 downstream of the stator blade.

In this research, the verification of the mesh number of the NASA stage 35 will carry out at the design speed. The number of grid nodes in the rotor blade tip clearance along the spanwise is 33. The mesh number of the single passage is verified from 1.14

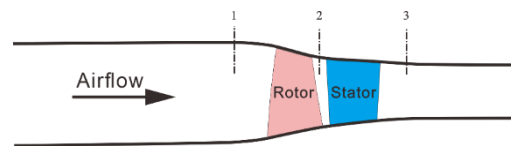
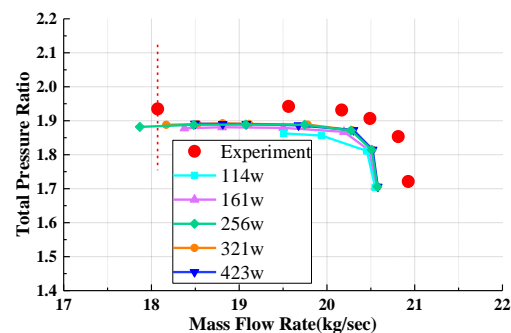


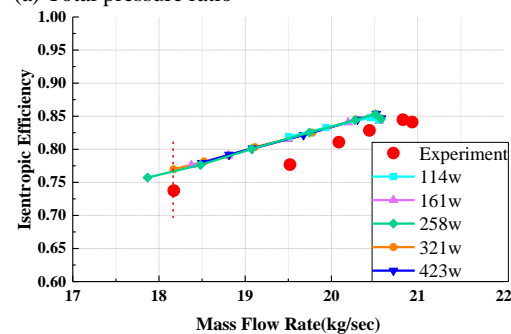
Fig. 3. Meridian plane and measurement positions of NASA stage 35.

million, which increases equally along the three directions each time. The variation trends of the characteristic lines (total pressure ratio and isentropic efficiency) of the axial compressor is shown in Fig. 4.

The capability of the mesh number owing 1.14 million in forecasting the total pressure ratio and the stall margin is weak. As the number of grids increases to 2.56 million or more, the predicted total pressure ratio remains basically unchanged, but the stall margin has not been accurately determined. In



(a) Total pressure ratio



(b) Isentropic efficiency

Fig. 4. Comparison of mesh numbers.

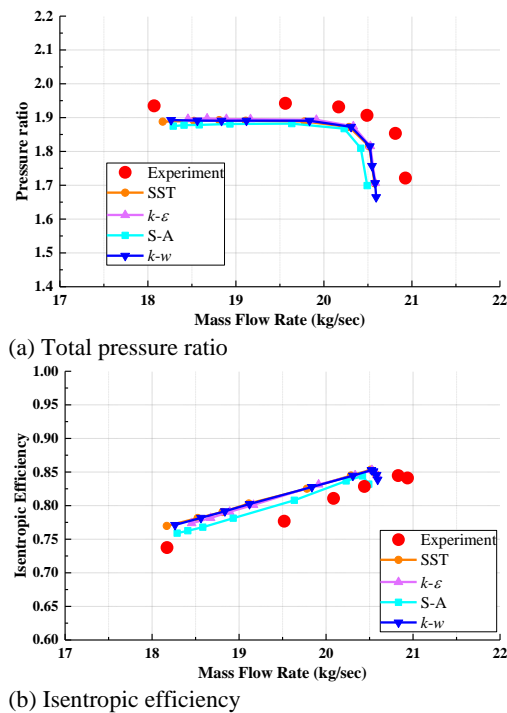


Fig. 5. Comparison of turbulence models.

addition, the changes in the mesh number show a small effect on the prediction of isentropic efficiency. The flow rate of the near-stall condition directly reflects the stable operating range of the compressor, and it is important for evaluating the compressor performance. For the impact of the mesh number on capturing the near-stall condition, it can be found that when the number of grids increases to 2.56 million, the stall margins become smaller and smaller, and when the number of grids increases from 2.56 to 4.23 million, the stall margins become larger. The stall margin of the compressor with a 3.21 million mesh number is consistent with the experimental result. Therefore, it is considered that the 3.21 million mesh number is the most suitable for the numerical study of NASA stage 35. The mesh number of the rotor is 1.76 million (including the inlet passage), and the mesh number of the stator is 1.45 million.

According to previous studies, the most commonly used turbulence models for turbomachinery simulation at present are the one-equation S-A model and the two-equation SST, $k-\epsilon$ and $k-w$ models. Figure 5 shows the characteristic lines of the calculated results of the four turbulence models and experimental results. The one-equation S-A model cannot accurately capture the near-stall condition. The obtained stable operating range is obviously too small, and the prediction of the total pressure ratio is significantly lower than the experimental value. Because the numerical calculation method does not consider the roughness of the walls, the steady calculation also does not consider the unsteady characteristic in real experiments. Therefore, there are still many uncertainties in the numerical simulation methods that result in errors. Although the total pressure ratio of the numerical results is lower than the experimental value, the overall trends

of the two equation models are consistent with the experimental values, and the near-stall condition captured by the SST turbulence model is closer to the experimental results.

Referring to the above verification results of the mesh number and turbulence model for the NASA stage 35 model, the SST turbulence model is applied to the 3.5-stage transonic axial compressor. The mesh number and topological construction are consistent with that of the NASA stage 35 modal. The mesh number of the NASA stage 35 excluding the inlet passage is 2.95 million. The “O4H” topology is also adopted.

The focus of this study is the last stage in a 3.5-stage transonic axial compressor. It is necessary to ensure that the number of grids in the last stage is about 2.9 million. Therefore, the mesh number of the last stage compressor is adjusted to 2.89 million. To save computational resources, the mesh number of the single passage in the other 2.5 stages is 1.76 million. Finally, the mesh number of the 3.5-stage axial compressor is 4.65 million.

4. STUDY OF THE AERODYNAMIC CHARACTERISTICS OF AN AXIAL COMPRESSOR

Previous studies found that when two flow control methods with different action positions were used to a cascade, the advantages of the two flow control methods were superimposed to improve the cascade performance for different aspects (Ma *et al.* 2019b, Karsten and Robert 2013). To further verify the previous research conclusions in a stage, a transonic multistage axial compressor is adopted, and the combined flow control technology is applied in a real stage environment.

Considering the fact that the research object of this work is a multistage axial compressor, the application of the flow control technologies not only affects the performance of the stator but also changes the flow fields of the rotor in the same stage. Therefore, to propose appropriate flow control methods can improve the aerodynamic performance of the compressor, the performance of the last stage in the multistage axial compressor should be taken for the evaluation of the flow control methods.

The total pressure ratio can directly reflect the capability to improve the pressure. This is also one of the classic definitions for evaluating the thermodynamic characteristics of a compressor. Therefore, the total pressure ratio of the last stage can be defined according to the extraction sections given in Fig. 1:

$$\pi_{13} = \frac{Pt_{RS_3}}{Pt_{RS_1}} \quad (1)$$

The subscript 13 indicates the data are extracted from planes RS_1 and RS_3 . The subscripts RS_3 and RS_1 represent the sections where the data is extracted. When the compressor works on the airflow, part of the mechanical work is used to increase the static

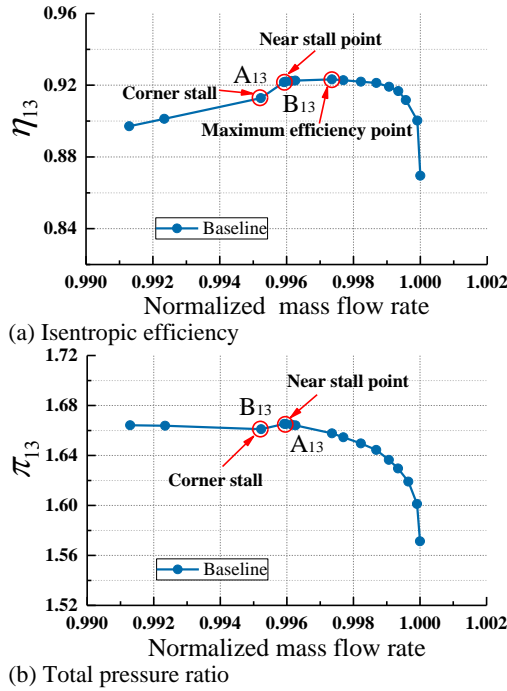


Fig. 6. Numerical simulation characteristic lines of the last stage in the axial compressor.

pressure, and the other part is consumed. Isentropic efficiency is the most common standard used to measure the utilization ratio of a compressor for mechanical power. The simplified formula for the last stage is as follows:

$$\eta_{13} = \frac{\pi_{13}^{\frac{k-1}{k}} - 1}{\frac{T_{RS_3}}{T_{RS_1}} - 1} \quad (2)$$

Figure 6 displays the aerodynamic characteristics of the last stage in the 3.5-stage transonic axial compressor. For the leftmost operating point, the compressor is still working, which is not the near-stall point of the 3.5-stage axial compressor. In this study, the stall characteristics of a multistage axial compressor are not the main focus, so the near-stall condition of the 3.5-stage compressor is not determined according to the detailed analysis. The abscissas are the normalized mass flow rate (\dot{m}) distribution based on the choking point of the baseline. The ordinates are the isentropic efficiency η_{13} and total pressure ratio π_{13} , respectively. As exhibited in Fig. 6 (a), the maximum efficiency point is reached soon when the flow rate gradually decreases. When \dot{m} is smaller than the value of point B₁₃, the isentropic efficiency suddenly drops to point A₁₃. As the airflow decreases further, the isentropic efficiency shows a significant decrease trend. When \dot{m} is less than the value of point B₁₃, the total pressure ratio also shows a sharp decrease in Fig. 6 (b), which indicates that the flow characteristics of the compressor deteriorate suddenly from point B₁₃ to point A₁₃.

In order to further analyze the compressor flow characteristics, it is necessary to locate the specific

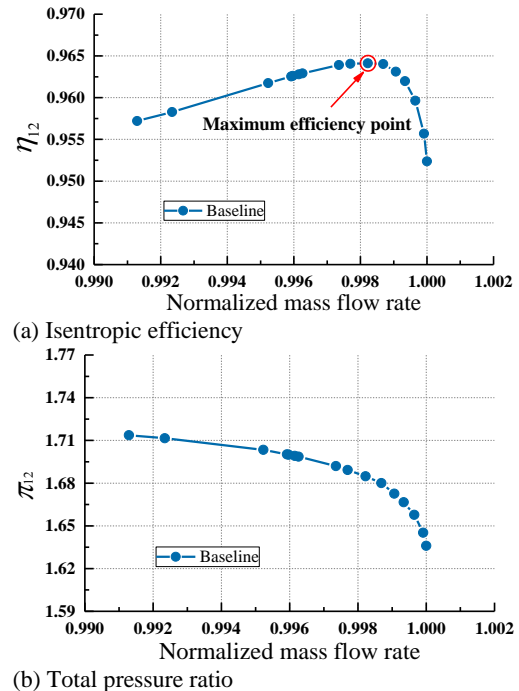


Fig. 7. Numerical simulation characteristic lines of the Rotor3 of the last stage in the axial compressor.

operating conditions where sudden changes occur in the flow field. Therefore, the aerodynamic performances of the rotor and the stator in the last stage are discussed separately. For the isentropic efficiency η_{12} and total pressure ratio π_{12} of the rotor in the last stage, the positions of data extraction are RS₁ and RS₂ in Fig. 1. The aerodynamic characteristic line of Stator 3 in the last stage is given in Fig. 7. As the flow rate decreases, the isentropic efficiency gradually decreases after reaching the highest point, and the decline process is gentle without the sudden drop. The total pressure ratio increases slowly with the decrease in the flow rate, and the sudden decrease also cannot be found.

The total pressure loss coefficient ζ_{RS2} can reflect the aerodynamic performance of the stator (Stator 3). The RS₂ section in Fig. 1 is defined as the inlet boundary of the stator. The definition of ζ_{RS2} is shown in Formula (3).

$$\zeta_{RS2}(x, y, z) = \frac{Pt_{RS2} - Pt(x, y, z)}{Pt_{RS2} - P_{RS2}} \quad (3)$$

Figure 8 shows the characteristic of ζ_{RS2} with the flow rate. As the airflow decreases, the ζ_{RS2} quickly decreases to the minimum loss point C₂₃ and then slowly increases to B₂₃. When the flow rate continues to decrease, the ζ_{RS2} rapidly increases to A₂₃, and then the value increases faster. This characteristic line further confirms that the sudden decrease of the total pressure ratio and the isentropic efficiency of the last stage is due to the performance change of Stator 3. It can be preliminarily determined that a deteriorated flow field occurs in Stator 3, and the corresponding condition is point A₂₃ in Fig. 8. Therefore, the

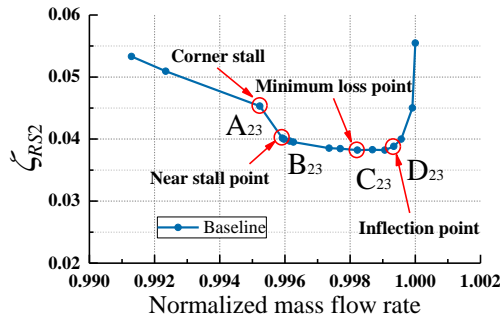


Fig. 8. Variation of total pressure loss coefficient with the flow rate.

following research discussion mainly focuses on Stator 3.

To further determine a corner stall, a detailed analysis of the flow field structure in a stator is required. The four representative flow fields in Fig. 8 are extracted and named corner stall point A_{23} , near-stall point B_{23} , minimum total pressure loss point C_{23} , and compressor performance inflection point D_{23} . The internal flow characteristics of the stator at each operating point are illustrated in Fig. 9. The ζ_{RS2} cloud is obtained at the cross-section of the TE, and the three-dimensional ranges covered by blue iso-surface are reverse flow regions.

The saddle point S_2 represents the starting position of the 3D corner separation (the region can be identified

by the reverse flow region), and the red dotted lines mean the separation lines. As the more low-energy fluid accumulates, node N_2 is formed on the end wall. The decrease in the airflow leads to an increase of incidence. From (a) to (c) in Fig. 9, with the gradual decrease of the flow rate, the accumulated low-energy fluid gradually increases and the starting position of the corner separation point S_2 gradually moves upstream. When the flow rate decreases to operating point B_{23} , the starting position of the corner separation point still stays at the 3D corner region, which indicates that the flow field is still stable.

When the flow rate decreases to point A_{23} , the point S_2 is in contact with the LE, and the starting position of the separation line suddenly departs from the corner region (saddle point S_2) and moves upward along the spanwise direction. At this time, the three-dimensional separation region becomes an open separation region. The range of the separation region shows significant enlargement in both the streamwise and spanwise directions, which indicates that the stator has entered an unstable operating condition (Ma *et al.* 2019a). The corner stall of the stator is caused by the accumulated low-energy fluid inside the corner region, which is also an important factor in the sudden increase of ζ_{RS2} (Fig. 8). The detailed analysis further verifies the fact that the corner stall occurs in the stator for the A_{23} condition.

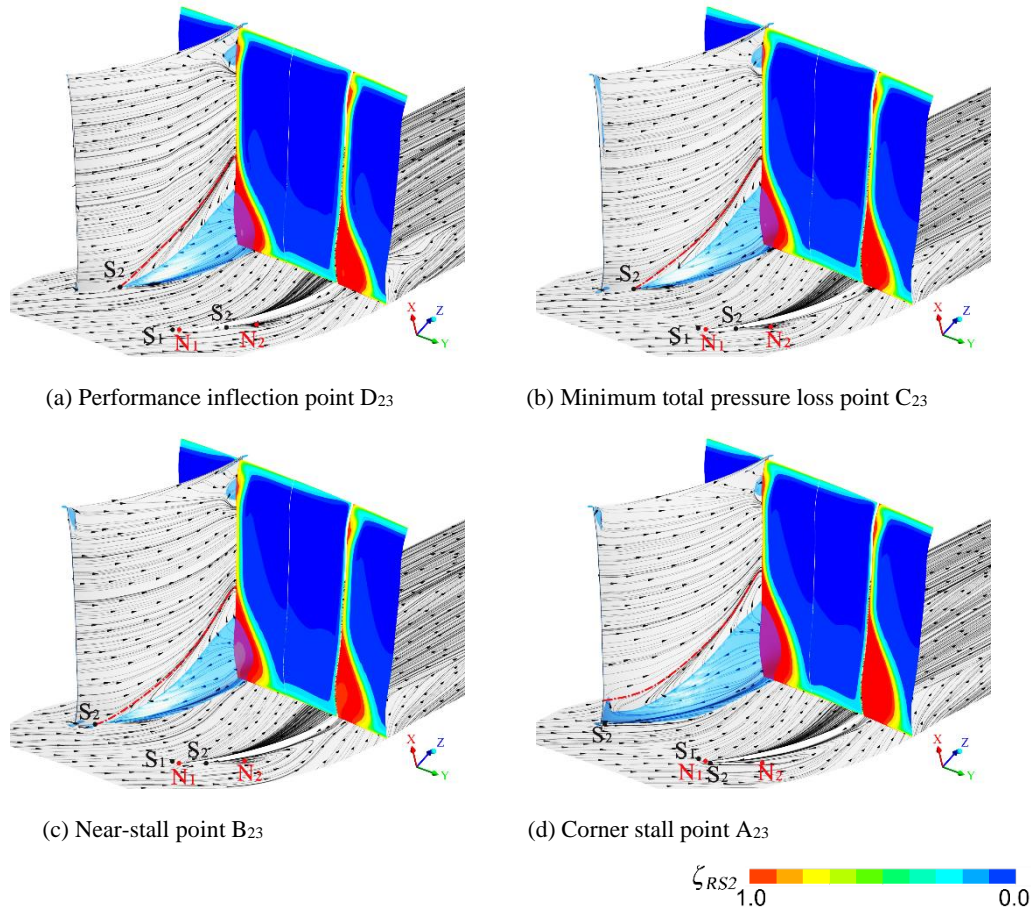


Fig. 9. Changes of reverse flow region and limiting streamline with flow rate.

5. INTRODUCTION OF THE FLOW CONTROL METHODS

Based on the analysis presented in section 4, the compressor can keep working after the occurrence of the corner stall in the stator of the last stage, but the performance shows an obvious deterioration trend. The main research object of this paper is the corner separation/stall of the stator, so the changes in the flow field performance are focused on in this section when the stator corner stall occurs.

In this research, the effects of flow control strategies on the performance of axial compressors are discussed. The flow control methods include micro-vortex generators (passive flow control) and boundary layer suction (active flow control). The geometric parameters and installation positions of the micro-vortex generator refer to [Ma *et al.* \(2019b\)](#) and [Ma *et al.* \(2021\)](#), and the shape is a trapezoidal structure with curvature. According to a large number of previous research results ([Lee and Loth 2009](#); [Santner *et al.* 2010.](#)), the height of the MVG is related to the thickness of the incoming boundary layer. Figure 10 shows the dimensionless velocity distribution along the spanwise direction at the inlet boundary of Stator 3 (RS₂ section in Fig. 1). The velocity of the 50% blade height is defined as the mainstream velocity V_m , and the boundary layer thickness δ near the hub is 0.13 times the blade height.

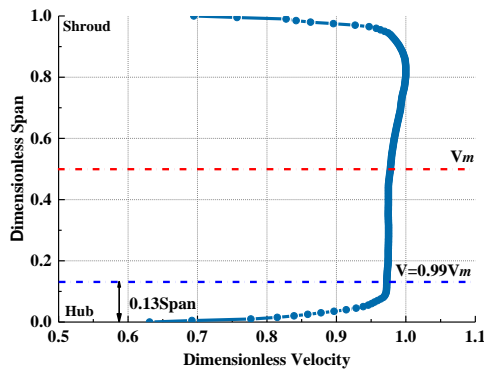


Fig. 10. Inlet velocity along the spanwise.

As shown in Fig. 11, the MVG is installed on the end wall in front of the blade passage. The trailing edge height h_T of the MVG is defined as 0.2 times the incoming boundary layer thickness ($h_T=0.2\delta$). The chord length of the MVG is $l_{VG}=h_T$, the blade space of the MVG is $d_{VG}=h_T$, the blade profile angle θ_{VG} is 30° , and the stagger angle β_{VG} is 36° . The axial distance l between the MVG and LE is 0.06 times the chord length, and the pitchwise distance d from the suction surface of the blade is 0.3 times the pitch. The red rectangles on the blade suction surface represent the location of the suction slot. To simulate the real suction process, the calculation domain includes the plenum and the suction slot. The top view of the blade, plenum, and the suction slot is shown in Fig. 12. The Z_{BLS} represents the axial installation position of the slot. In the enlarged view, the width is 1% of the axial chord length, which is represented by w_{BLS} .

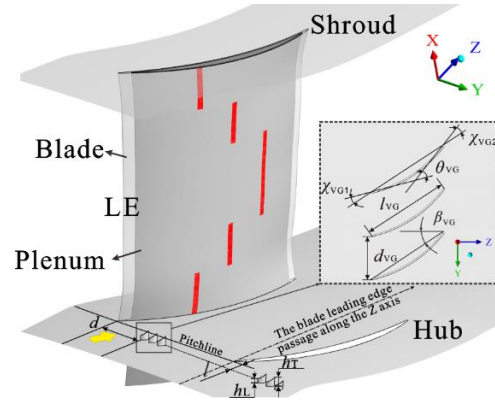


Fig. 11. Geometric structure of vortex generator and suction slot.

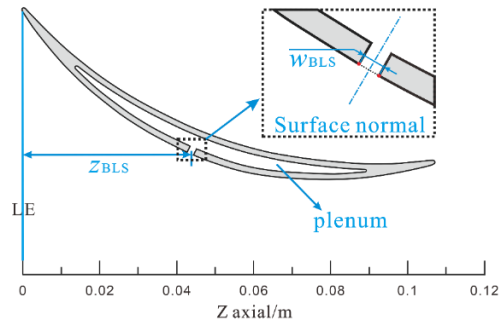


Fig. 12. Top view of the blade with plenum and slot.

Refers to the literature reference [Ma *et al.* \(2021\)](#), a segmented suction slot is selected in this research. Figure 13 shows the distribution of the segmented suction slots. The airflow is sucked in the plenum by the five section suction slots, and the airflow out of the plenum has a 1% suction mass-flow ratio. The axial position of the upper and lower suction slots near the LE is set at a 30% axial chord length, and the height of the slots is 1/6 of the blade height. The height of the two suction slots at the 50% axial chord length is also 1/6 of the blade height, which is closer to the mid-span. The two suction slots located at 70% of the axial chord length also have a 1/6 blade height and are connected into one slot, so the height is 1/3 of the blade height.

The mesh and boundary conditions of Stator 3 with the MVG_{CT} and BLS_{Sec} are given in Fig. 14, and the grid topology is shown in the partially enlarged views. The blade is surrounded by O-type grid topology, and the plenum is filled by a butterfly grid, which is presented in the partially enlarged views of *a* and *b*. As shown in the enlarged views *c* and *d*, the grids near the MVGs and suction slots are locally densified. The first layer grid near the wall needs to be set to 1×10^{-6} m, which can guarantee that the near wall $y^+ < 1$. The outlet boundary of the plenum (the red boundary in Fig. 14) is static pressure, and a proper static pressure can ensure a 1% suction mass-flow ratio. The walls of the MVGs and suction slots are set as no-slip walls. The General Connection interface is used between the suction slot and the blade suction surface. The General Connection interface model of the commercial software CFX is

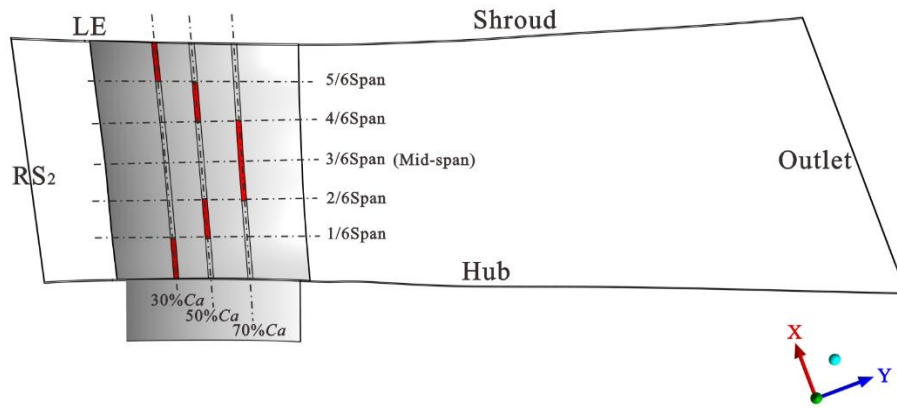


Fig. 13. Distributions of suction slots on blade suction surface.

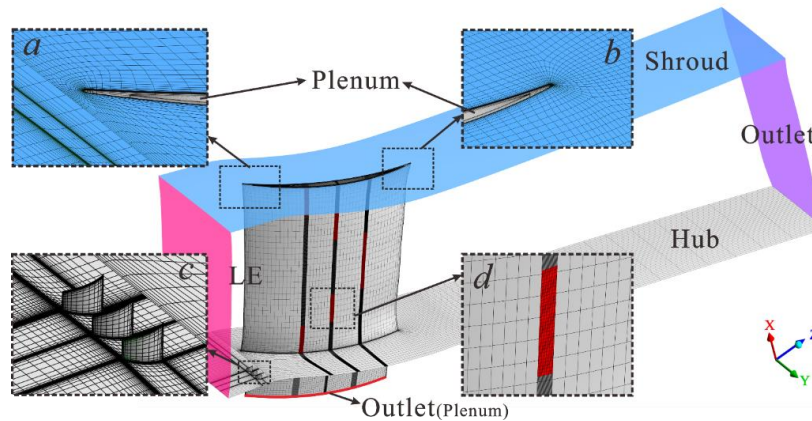


Fig. 14. Mesh of Stator 3 with MVG_{CT} and BLS_{Sec}.

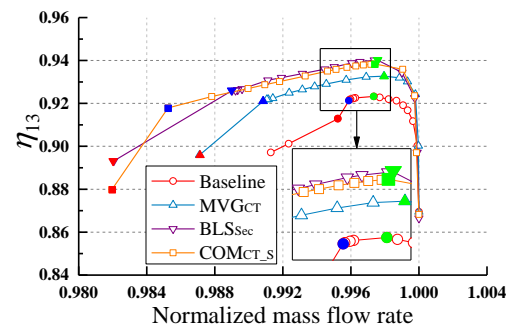
an effective way to connect regions and it can be used to connect non-matching grids.

6. EFFECTS OF ACTIVE/PASSIVE FLOW CONTROL TECHNOLOGIES ON AXIAL COMPRESSOR PERFORMANCE

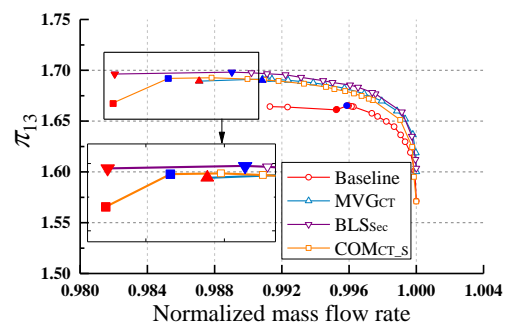
6.1 Performance of the Last Stage

The flow control methods can improve the aerodynamic performance of a stator, and the influence of the compressor stage performance should not be ignored in the research process. Therefore, Fig. 15 compares the influences of different flow control methods on the aerodynamic characteristics of the last stage. The stator using the micro-vortex generator only is represented by MVG_{CT} (Micro-vortex generator with curved trapezoid), the stator applying the segmented suction slot only is represented by BLS_{Sec} (Segmented boundary layer suction), and the stator with both the MVG and the segmented suction slot is represented by COM_{CT,S} (Combined technologies between MVG_{CT} and BLS_{Sec}). Part of the low speed flow in the passage is aspirated by the suction slot, which leads to the characteristic lines moving to the low flow rate condition. The mass flow rate (\dot{m}) is normalized by the choking point itself. The characteristic lines of the baseline are normalized by the choking point of the baseline, and the characteristic lines of MVG_{CT} are normalized by the choking point of MVG_{CT} and so on. This makes the

characteristic lines of the different cases easy to compare and analyze.



(a) Isentropic efficiency



(b) Total pressure ratio

Fig. 15. Effects of flow control technologies on the last stage performance of the axial compressor.

The forecast results of the near-stall points (blue solid points) and stall points (red solid points) of different research cases are given in Fig. 15, and the highest efficiency points are represented by the green solid points. It can be found that different flow control technologies can improve the aerodynamic characteristic of the last stage, and the total pressure ratio and isentropic efficiency show an increasing trend. When the corner stall of the stator occurs, the values of isentropic efficiency and the stage pressure ratio in the last stage decrease suddenly (Fig. 15 (a) and the enlarged view in Fig. 15 (b)). Therefore, it can be inferred that the corner stall of the baseline occurs at the red operating points in Fig. 15.

MVG_{CT} shows a weaker capability to improve the pressure ratio and isentropic efficiency and delay the corner stall compared with the BLS_{Sec} and COM_{CT-S}. Although the pressure ratio and efficiency of COM_{CT-S} are slightly lower than those of BLS_{Sec}, it shows an advantage in delaying the occurrence of a corner stall.

To measure the stable operating range and evaluate the safety of the compressor, the stability margin needs to be introduced. At present, the surge margin (*SM*) is widely applied to evaluate the stall margin of a compressor. It takes into account the combined effects that is the flow rate and total pressure ratio. The defined *SM* is given as follows:

$$SM = \left(\frac{\pi_s / \dot{m}_s}{\pi_0 / \dot{m}_0} - 1 \right) \times 100\% \quad (4)$$

The research focus of this paper is the use of flow control technologies to improve the aerodynamic characteristics of an axial compressor. Therefore, the performance improvement of an optimized compressor is of further concern. Improvements in the stall margin and peak efficiency are often adopted to evaluate the optimization degree of compressor performance, and these are the important criteria for measuring the optimization methods.

The stall margin improvement ΔSM can be obtained as follows:

$$\Delta SM = \left[\left(\frac{\pi_{IM}}{\pi_{BS}} \right)_s \cdot \left(\frac{\dot{m}_{BS}}{\dot{m}_{IM}} \right)_s - 1 \right] \times 100\% \quad (5)$$

The formula of peak efficiency improvement $\Delta \eta_e$ is as follows:

$$\Delta \eta_e = \left[\frac{(\eta_e)_{IM}}{(\eta_e)_{BS}} - 1 \right] \times 100\% \quad (6)$$

Referring to the research works of Sun *et al.* (2021b) and Sun *et al.* 2020, the airflow flows out from the suction slot should be reutilized, and the corresponding adiabatic efficiency η_{13suc} should be considered. η_{13suc} is defined as shown in Eq. (7).

$$\eta_{13suc} = \frac{(1 - \dot{m}_{suc}) \cdot (\pi_{13}^{\frac{k-1}{k}} - 1) + \dot{m}_{suc} \cdot (\pi_{suc}^{\frac{k-1}{k}} - 1)}{(1 - \dot{m}_{suc}) \cdot \left(\frac{T_{RS3}}{T_{RS1}} - 1 \right) + \dot{m}_{suc} \cdot \left(\frac{T_{RS3}}{T_{suc}} - 1 \right)} \quad (7)$$

Table 2 Performance improvements of the last stage in the axial compressor.

Fluid control schemes	ΔSM	$\Delta \eta_e$	$\Delta \eta_{esuc}$
MVG _{CT}	2.1%	1.02%	-
BLS _{Sec}	2.69%	1.83%	3.62%
COM _{CT-S}	2.71%	1.63%	3.42%

Therefore, the peak efficiency improvement $\Delta \eta_{esuc}$ considering the suction flow is given in Eq. (8).

$$\Delta \eta_{esuc} = \left[\frac{(\eta_{esuc})_{IM}}{(\eta_{esuc})_{BS}} - 1 \right] \times 100\% \quad (8)$$

In order to quantitatively measure the improvements of flow control methods on the aerodynamic characteristic of the last stage, Table 2 shows the improvements of the stall margin ΔSM , peak efficiency $\Delta \eta_e$ and $\Delta \eta_{esuc}$. The data are extracted from planes RS₁ and RS₃. The MVG_{CT} shows a certain advantage in improving the compressor performance, but it is weaker in improving the efficiency and stable operating range compared with the BLS_{Sec} and COM_{CT-S}. Moreover, the COM_{CT-S} shows a powerful ability in expanding the stable operating range, and the stall margin improvement reaches 2.71%. BLS_{Sec} presents an obvious advantage in enhancing the isentropic efficiency. The peak efficiency improvement $\Delta \eta_e$ is 1.83 % and the $\Delta \eta_{esuc}$ considering the suction flow reaches 3.62%.

6.2 Performance of Stator 3

The influences of different flow control technologies on the performance of a compressor have been preliminarily explored. The following discussion focuses on the improvements in the performance of the last stage stator by the flow control technologies. Figure 16 shows the incidence characteristic lines of the stator. The red solid points are the stall conditions, and the near-stall conditions are represented by the blue solid points. The green solid points represent the minimum loss points, and the orange solid point represents the performance inflection point of the baseline. To further analyze the advantages of the flow control technologies in

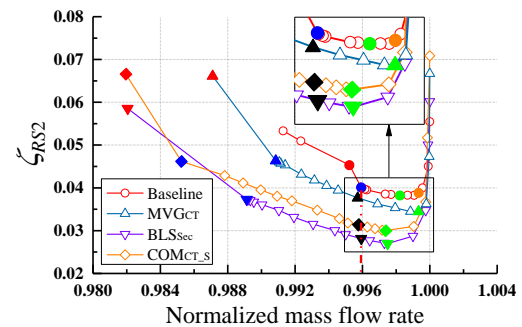


Fig. 16. Effects of flow control technologies on the stator performance of the last stage.

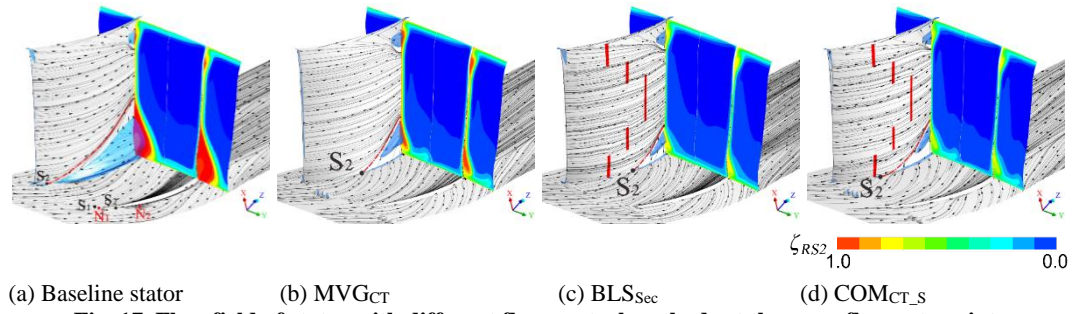


Fig. 17. Flow field of stator with different flow control methods at the same flow rate point.

improving the compressor's characteristics, the flow fields of the stator using different flow control technologies at the same flow rate point are compared. Therefore, the flow fields of the MVGCT, BLS_{sec} and COM_{CT,S} at the same flow rate point (the near-stall point of the baseline) are discussed, and the conditions can be found in Fig. 16 (the black solid points). These three points are called the same flow rate conditions.

As given in Fig. 16, the ζ_{RS2} of the stator with the three flow control technologies is significantly reduced under all operating conditions, and the stable operating range is widened. The combined technology COM_{CT,S} shows a weak capability in reducing the ζ_{RS2} compared with the BLS_{sec}, but it has a significant advantage in delaying the occurrence of a corner stall. To further analyze the influences of flow control schemes on the compressor's performance, the internal flow field structure of the stator passage is analyzed in detail.

Figure 17 compares the effects of three flow control methods on the stator passage at the same flow rate point. The BLS_{sec} has an advantage in aspirating the three-dimensional reverse flow region (blue iso-surface) and reducing the total pressure loss (ζ_{RS2} cloud extracted on the cross-section of TE) in Fig. 17 (c). Although the MVGCT can also effectively improve the flow field (Fig. 17 (b)), its capacity is inferior compared with the BLS_{sec}. When the MVGCT is applied in the stator with the segmented suction slot (COM_{CT,S}, Fig. 17 (d)), the flow field shows slight deterioration compared with the BLS_{sec}. The corner separation is expanded and the ζ_{RS2} is enhanced. If excessive low-energy fluid accumulates in the 3D corner region, the MVGCT and BLS_{sec} can effectively improve the flow field characteristics. However, if the accumulation of the low-energy fluid is not serious (similar to BLS_{sec}), the introduction of MVG will deteriorate the stator performance.

The effect of suction power on the compressor performance should also be considered (Ma *et al.* 2019b). The corresponding total pressure loss coefficient ζ_{suc} is given in Eq. (9).

$$\zeta_{suc} = \frac{(1 - \dot{m}_{suc}) \cdot (Pt_{RS2} - Pt_{RS3}) + \dot{m}_{suc} \cdot (Pt_{RS2} - Pt_{suc})}{Pt_{RS2} - P_{RS2}} \quad (9)$$

Moreover, the diffusion factor (DF) can be used to evaluate the expanding degree of stator passage. The definition of the DF is provided as follows:

Table 3 Performance improvements of Stator 3.

Cases	ζ_{RS2}	ζ_{suc}	DF
Baseline	0.0402	-	0.41
MVGCT	0.0377	-	0.48
BLS _{sec}	0.0282	0.0449	0.50
COM _{CT,S}	0.0314	0.0483	0.50

$$DF = 1 - \frac{w_{TE}}{w_{LE}} + \frac{\Delta w_u}{2w_{LE}\tau} \quad (10)$$

The main aerodynamic parameters of the four cases at the same flow rate points are compared in Table 3. The values of ζ_{RS2} are consistent with Fig. 16. Fouce on the ζ_{suc} considering the effect of aspirated airflow, the loss of COM_{CT,S} is still higher than that of BLS_{sec}. When some flow control schemes are introduced in the baseline, the DFs are significantly enhanced, and the BLS_{sec} and COM_{CT,S} show a significant advantage in improving the expanding degree of the stator passage.

To quantitatively compare the impacts of different flow control methods on the compressor performance, this paper refers to previous research methods (Li *et al.* 2014, 2017) to classify the flow loss in the blade passage. The three-dimensional passage is divided into several sub-domains based on the causes of the blockage. Each sub-domain corresponds to a type of loss mechanism according to the causes of the local blockage. The evaluation method of the cascade blockage proposed by Khalid (1995) is adopted to obtain the blockage distribution, which is calculated using the scalar $\nabla(\rho v_m)$. However, the boundary of the local blocking range needs to be reflected in a cross-section perpendicular to the streamwise direction, and the spanwise and pitchwise gradient components of the $\nabla(\rho v_m)$ can be used to calculate the gradient magnitude. For the cylindrical coordinate system, the gradient magnitude is expressed as $|\nabla(\rho v_m)|_{r,\theta}$. Khalid proposed after a large amount of research for the normalized formula, the contour line with a value of 2 is defined as the blockage boundary, and the range bigger than 2 was defined as the blocking range. The normalized blockage boundary was defined as follows:

$$|\nabla[\rho v_m]|_{r,\theta} / (\rho_{in} v_{in,c} / C) = 2 \quad (11)$$

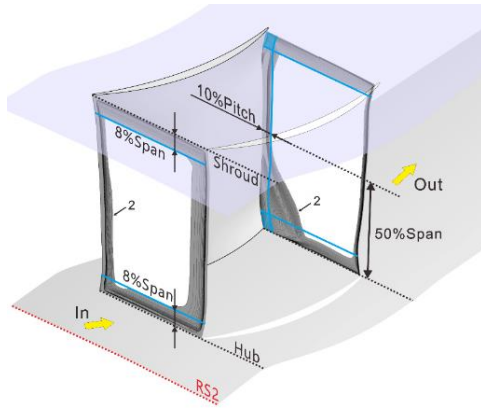


Fig. 18. Distributions of the blockage.

Before the incoming flow enters the blade passage, the boundary layer is not affected by the reverse and pitchwise pressure gradient. Therefore, the main flow direction on the chordwise section of the LE is consistent with the flow direction at the inlet boundary. The average airflow angle (the angle between the incoming flow and the Z-axis) at the inlet section RS_2 of Stator 3 is 37.85° . The designed exit flow angle of Stator 3 is parallel to the chordwise direction, so it is considered that the main flow direction on the chordwise cross-section of the TE is consistent with the chordwise direction.

According to Khalid, the blockage distributions on the cross-section of the LE and TE are shown in Fig. 18 (design condition). In the figure, the gray iso-surfaces located on the cross-sections represent the two-dimensional blocking range. When the airflow is not entering the blade passage, the blockages near the end walls (hub and shroud) are mainly from the boundary layer's viscous effect. According to the blockage distribution on the cross-section of the LE, the spanwise range between the end wall and the blockage boundary (blue line) is defined as the end wall loss range. Based on Fig. 18, the heights of the end wall loss range near the hub and shroud have an 8% span.

When the airflow reaches the TE, the viscous effect between the airflow and the blade is fully developed. According to previous studies (Hergt *et al.* 2006), the airflow near the mid-span is the least influenced by the secondary flow and end wall. Therefore, the blockage at the mid-span is mainly caused by the

viscous effect of the blade surface, and the O-type block surrounding the blade is defined as the profile loss range. As shown in Fig. 18, the pitchwise range of the O-type block is about a 0%-10% pitch. Furthermore, the corner vortex is also the main vortex structure causing the flow loss. Therefore, it is necessary to account for the corner loss. To facilitate the calculation, the O-type block surrounded by the blue rectangle is defined as the corner blocking range in Fig. 18.

According to the classification of flow loss, Fig. 18 shows a regional division of the three-dimensional flow field. The corresponding flow losses include seven parts, and each part of the loss corresponds to a kind of loss source. The loss sources are classified as follows:

γ_{Pro} (profile loss): The loss source is mainly due to the viscous effect from the blade.

γ_{Sec} (secondary flow loss): The loss source mainly comes from the interior of the blade passage, such as the shearing between the flow separation and the mainstream.

γ_{Wake} (wake loss): As the airflow leaves the TE of the blade, the loss source is induced by the mixing effect between the low-energy fluid (blade suction side) and the main flow (blade pressure side) and the dissipation of the low-energy fluid.

γ_{Com_Hub} (corner loss near the hub) and γ_{Com_Shr} (corner loss near the shroud): The loss sources are produced by the corner vortex and the boundary layer turning flow around the leading edge.

γ_{Wall_Hub} (end wall loss near the hub) and γ_{Wall_Shr} (end wall loss near the shroud): The loss sources are mainly due to the viscous effect from the end wall (hub and shroud).

The detailed range of the different loss sources is listed in Table 4.

The "loss source" proposed by Li *et al.* (2014) is adopted to calculate the flow loss in the specific regions. This method uses a dissipation function to reflect the generation rate of the local flow loss. To obtain different local flow losses, volume integration is performed for the loss sources in the different three-dimensional flow field shown in Fig. 19.

Table 4 Spatial divisions based on the loss sources.

Loss sources	γ_{Pro}	γ_{Sec}	γ_{Com_Hub}	γ_{Com_Shr}
Streamwise range	LE-TE	LE-TE	LE-TE	LE-TE
Spanwise range	8% -92% span	8% -92% span	0% -8% span	92% -100% span
Pitchwise range	10% pitch away from the blade	Pitchwise range without the γ_{Pro}	10% pitch away from the blade	10% pitch away from the blade
Loss sources	γ_{Wall_Hub}	γ_{Wall_Shr}	γ_{Wake}	
Streamwise range	LE-TE	LE-TE	TE-Outlet	
Spanwise range	0% -8% span	92% -100% span	0% -100% span	
Pitchwise range	Pitchwise range without the γ_{Com}	Pitchwise range without the γ_{Com}	Full passage	

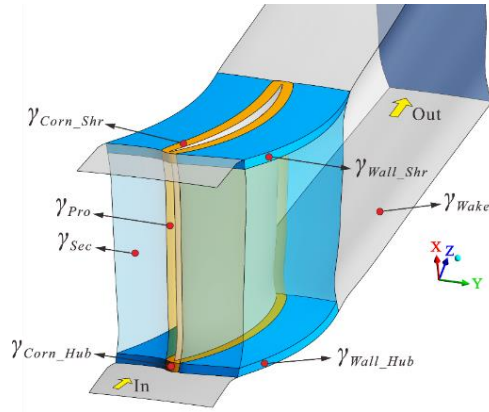


Fig. 19. Regional division of loss sources.

In a mechanical equation, the dissipation function Φ is the only term used to convert mechanical energy into heat energy. The dissipation function Φ is selected to evaluate the loss source. The definition of Φ is given as follows:

$$\Phi(x, y, z) = \frac{\mu_{\text{eff}}}{2} \left(\frac{\partial v_i}{\partial x_j} + \frac{\partial v_j}{\partial x_i} \right)^2 - \frac{2}{3} \mu_{\text{eff}} \left(\frac{\partial v_i}{\partial x_i} \right)^2 \quad (12)$$

The viscosity coefficient of the fluid is modified as follows:

$$\mu_{\text{eff}} = \mu + \mu_t \quad (13)$$

The effective viscosity coefficient μ_{eff} is the sum of μ and μ_t (laminar viscosity coefficient and turbulent viscosity coefficient). The expression of the loss source corresponding to the different regions is obtained as follows:

$$\gamma_{\text{source}} = \frac{\Delta P t_{\text{source}}}{P_{t_{\text{in}}} - P_{\text{in}}} = \frac{\iiint_{\text{region}} \Phi dx dy dz}{(P_{t_{\text{in}}} - P_{\text{in}}) \iint_{\text{in}} v \cdot n dA} \quad (14)$$

Figure 20 displays the proportions of the different loss sources in the baseline Stator 3 at the minimum loss point (Fig. 9 (b)). It is found that the wake loss source is the main component of the loss source in

the stator calculation domain, and the proportion reaches 32%. Furthermore, due to the effect of the corner separation near the hub, the loss sources near the hub ($\gamma_{\text{Corn_Hub}}$ and $\gamma_{\text{Wall_Hub}}$) are bigger than the loss sources near the shroud ($\gamma_{\text{Corn_Shr}}$ and $\gamma_{\text{Wall_Shr}}$).

Focused on the proportion of each loss source in the baseline Stator 3, Fig. 21 compares the effects of the three flow control technologies on the different loss sources at the minimum loss point. The ordinate represents the variations of the different loss sources. Based on the histogram, it can be found that the three methods show significant advantages to reducing the secondary flow loss sources γ_{Sec} and wake loss sources γ_{Wake} . The secondary flow loss sources of the MVGCT, BLS_{Sec} and COMCT_S are decreased by 49.23%, 52.66%, and 52.86%, respectively. The wake loss sources are decreased by 12.02%, 33.06%, and 27.64%, respectively.

For the BLS_{Sec}, most of the loss sources are significantly reduced, only the reduction of the secondary flow loss source shows certain inferiority compared with the COMCT_S. Due to the introduction of the suction slot, the disturbance is increased, which enhances the shear effect in the corner region near the hub, so the corner loss sources near the hub $\gamma_{\text{Corn_Hub}}$ are enhanced. For the MVGCT, due to the influence of the installation position, the flow shear effect near the hub is more obvious, which significantly increases the end wall loss source near the hub $\gamma_{\text{Wall_Hub}}$ and slightly increases the blade profile loss source γ_{Pro} .

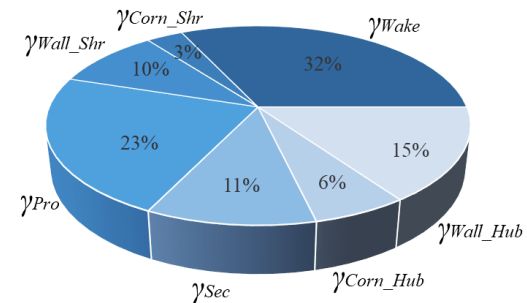


Fig. 20. Proportion of each loss source in Stator 3 at the minimum loss point.

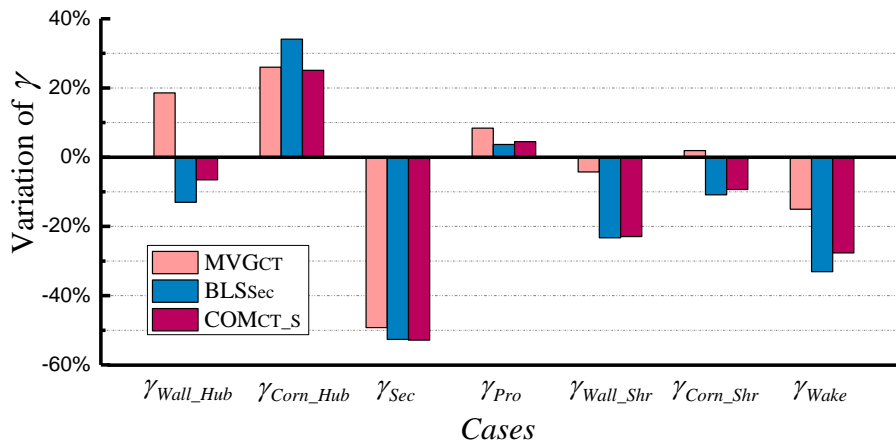


Fig. 21. Effect of flow control technologies on local loss sources at the minimum loss point.

7. CONCLUSION

To explore the characteristics of different flow control methods in a stage environment, a 3.5-stage transonic axial compressor is the research object. Some conclusions are summarized as follows:

(1) The corner stall of the compressor stator is directly caused by the excessive accumulation of reverse flow. With the decrease of the flow rate, the reverse flow in the corner region of the compressor stator gradually appears to have excessive accumulation. If the last stage stator of the compressor enters the corner stall state in the beginning, the corner separation in the stator suddenly transforms into an unstable flow structure, which does not cause the compressor to surge instantly, but the performance has accelerated deterioration. If the corner separation of the stator can be effectively suppressed by some flow control methods, the aerodynamic performance of the compressor can be recovered.

(2) When the three flow control technologies are used in the stator, the total pressure loss coefficients are significantly reduced under all operating conditions, and the stable operating range is widened. MVG_{CT} can effectively improve the flow field characteristics, but its capacity is inferior compared with that of the BLS_{Sec}. The BLS_{Sec} shows a significant advantage, the stall margin improvement of the last stage is 2.69% and the peak efficiency improvement $\Delta\eta_e$ is 1.83%. However, when the COM_{CT,S} is applied, it shows a significant advantage to delay the occurrence of a corner stall, and the stall margin of the last stage is improved by 2.71%.

(3) Based on the loss source analysis method, the three flow control schemes show significant advantages in reducing the secondary flow loss sources and wake loss sources. The secondary flow loss sources of the MVG_{CT}, BLS_{Sec} and COM_{CT,S} are decreased by 49.23%, 52.66%, and 52.86%, respectively, and the wake loss sources are decreased by 12.02%, 33.06%, and 27.64%, respectively.

ACKNOWLEDGEMENTS

This study was co-supported by the financial support of the National Science Fund for Distinguished Young Scholars (52206063), Sichuan Natural Science Foundation for Distinguished Young Scholars (23NSFSC2925 and 2022NSFSC1894), Civil Aviation Flight University of China Scientific Research Fund (J2022-001).

REFERENCES

Alexander, H., R. Meyer, K. Liesner and E. Nicke (2011). A new approach for compressor endwall contouring. In *Proceeding of ASME Turbo Expo*, British Columbia, Canada.

Chima, R. V. (2009). SWIFT code assessment for two similar transonic compressors. In *47th*

AIAA Aerospace Sciences Meeting including The New Horizons Forum and Aerospace Exposition, American Institute of Aeronautics and Astronautics.

- Dawen, X., C. Zihua, J. Xiaohai and F. BaoChun (2014). Numerical investigations on the wake structures of micro-ramp and micro-vanes. *Fluid Dynamics Research* 46(1), 015505.
- Dejour, Q. and H. D. Vo (2018). Assessment of a Novel Non-Axial Counter-Rotating Compressor Concept for Aero-Engines. In *Proceeding of ASME Turbo Expo*, Oslo, Norway.
- Diaa, A. M., M. F. El-Dosoky, O. E. Abdel-Hafez and M. A. Ahmed (2014). Secondary flow control on axial compressor cascade using vortex generator. In *Proceedings of the ASME 2014 International Mechanical Engineering Congress and Exposition*, Montreal, Quebec, Canada.
- Ding, J., C. Shaowen, X. Hao, S. Sun, and S. Wang (2013). Control of flow separations in compressor cascade by boundary layer suction holes in suction surface. In *Proceedings of ASME Turbo Expo*, San Antonio, Texas, USA.
- Ding, J., D. Xin, C. Shaowen, X. Zhou, S. Wang and J. Shen (2017). Influence of Tailored Boundary Layer Suction on Aerodynamic Performance in Bowed Compressor Cascades. In *Proceedings of ASME Turbo Expo*, Charlotte, NC, USA.
- Godard, A, F. Bario, S. Burguburu and F. Leboeuf (2012). Experimental and numerical study of a subsonic aspirated cascade. In *Proceeding of ASME Turbo Expo*, Copenhagen, Denmark
- Hergt, A., R. Meyer and K. Engel (2006). Experimental investigation of flow control in compressor cascades. In *Proceeding of ASME Turbo Expo*, Barcelona, Spain.
- Hergt, A., R. Meyer, M. W. Müller (2008). Loss reduction in compressor cascades by means of passive flow control. In *Proceeding of ASME Turbo Expo*, Berlin, Germany.
- Jonas, M., S. Gantner, J. Ståding and J. Friedrichs (2018). A machine learning based approach of performance estimation for high-pressure compressor airfoils. In *Proceeding of ASME Turbo Expo*, Oslo, Norway.
- Karsten, L. and R. Meyer (2013). Evaluation of passive and active secondary flow control in a high speed compressor cascade with different measurement techniques. *Notes on Numerical Fluid Mechanics & Multidisciplinary Design* 121(9),125-133.
- Khalid, S. A. (1995). *The Effects of Tip Clearance on Axial Compressor Pressure Rise*. Doctoral dissertation, Massachusetts Institute of Technology.
- Lee, S. and E. Loth (2009). Supersonic boundary-layer interactions with various micro-vortex

- generator geometries. *AIAA Paper* 113, 683-697.
- Li, X. J., W. L. Chu and Y. H. Wu (2014). Numerical investigation of inlet boundary layer skew in axial compressor cascade and the corresponding non-axisymmetric end-wall profiling. *Proceedings of the Institution of Mechanical Engineers, Part A: Journal of Power and Energy* 228(6), 638-656.
- Li, Z. Y., J. Du, A. Jemcov, X. Ottavy and L. Feng (2017). A study loss mechanism in a linear compressor cascade at the corner stall condition. In *Proceeding of ASME Turbo Expo*, Charlotte, NC, USA.
- Lin, J. C. (2002). Review of research on low-profile vortex generators to control boundary-layer separation. *Progress in Aerospace Sciences* 38(4-5), 389-420.
- Lin, J. C., G. V. Selby and F. G. Howard (1991). Exploratory study of vortex-generating devices for turbulent flow separation control. In *AIAA 29th Aerospace Sciences Meeting*, Hampton VA.
- Ma, S. W. Chu, H. Zhang, S. Yan and Y. Zhong (2019a). Study of combined flow control strategies based on a quantitative analysis in a high-load compressor cascade. *Aerospace Science and Technology* 93, 105346.
- Ma, S., W. Chu and X. Sun (2021). Effects of segmented layer suction and micro-vortex generator on a high-load compressor cascade performance. *Proceedings of the Institution of Mechanical Engineers, Part C: Journal of Mechanical Engineering Science* 235(21), 5309-5323.
- Ma, S., W. Chu, H. Zhang, X. Li and H. Kuang. (2019b). A combined application of micro-vortex generator and boundary layer suction in a high-load compressor cascade. *Chinese Journal of Aeronautics* 32(5), 1171-1183.
- Meng, Q., S. Chen, W. Li, et al. (2018). Numerical investigation of a sweeping jet actuator for action flow control in a compressor cascade. In *Proceeding of ASME Turbo Expo*, Oslo, Norway.
- Reid, L. and R. D. Moore (1978). *Performance of a Single-Stage Axial-Flow Transonic Compressor with Rotor and Stator Aspect Ratios of 1.19 and 1.26, Respectively, and with Design Pressure Ratio of 1.82*. NASA TP-1338.
- Saito, S., Y. Tamura, M. Furukawa, K. Yamada and N. Niwa (2018). Flow structure and unsteady behavior of hub-corner separation in a stator cascade of a multi-stage transonic axial compressor. In *Proceeding of ASME Turbo Expo*, Oslo, Norway.
- Santner, C., E. Gottlich, A. Marn, J. Hubinka and B. Paradiso (2010). The application of low-profile vortex generators in an intermediate turbine diffuser. *Journal of Turbomachinery* 134, 1445-1455.
- Smith, L. H. (2002). Axial compressor aerodesign evolution at general electric. *Journal of Turbomachinery* 124(3), 321-330.
- Stürzebecher, T., G. Goinis, C. Voss, H. Sahota, P. Groth and S. Hammer (2018). Automated aerodynamic optimization of an aggressive s-shaped intermediate compressor duct. In *Proceeding of ASME Turbo Expo*, Oslo, Norway.
- Sun, S., J. Hao, J. Yang, L. Zhou and L. Ji. (2021a). Impacts of tandem configurations on the aerodynamic performance of an axial supersonic through-flow fan cascade. *Journal of Turbomachinery* 1-25.
- Sun, S., S. Wang and S. Chen (2020). Design, modification and optimization of an ultra-high-load transonic low-reaction aspirated compressor. *Aerospace Science and Technology* 105, 105975.
- Sun, S., S. Wang, L. Zhang and L. Ji (2021). Design and performance analysis of a two-stage transonic low-reaction counter-rotating aspirated fan/compressor with inlet counter-swirl. *Aerospace Science and Technology* 111(3), 106519.
- Taylor, J. V. and R. J. Miller (2015). *Competing 3D Mechanisms* Proceeding of ASME Turbo Expo, Montréal, Canada
- Vanti, F., L. Pinelli, A. Arnone, A. Schneider and P. Astrua, Enrico Puppo (2018). Aeroelastic optimization of an industrial compressor rotor blade geometry. In *Proceeding of ASME Turbo Expo*, Oslo, Norway.
- Yue, S. and Y. Wang (2018). Design and optimization of tandem arranged cascade in a transonic compressor. *Journal of Thermal Science* 27(4), 349-358.